THE ASTROPHYSICAL JOURNAL, 520:880–894, 1999 August 1

CORONAL LOOP OSCILLATIONS OBSERVED WITH THE *TRANSITION REGION AND CORONAL EXPLORER*

MARKUS J. ASCHWANDEN, LYNDSAY FLETCHER, CAROLUS J. SCHRIJVER, AND DAVID ALEXANDER
Lockheed-Martin ATC, Solar and Astrophysics Laboratory, Department H1-12, Building 252, 3251 Hanover Street, Palo Alto, CA 94304; aschwanden@lmsal.com
Received 1999 January 6; accepted 1999 March 10

ABSTRACT

We report here, for the first time, on spatial oscillations of coronal loops, which were detected in extreme-ultraviolet wavelengths (171 Å) with the *Transition Region and Coronal Explorer*, in the temperature range of $T_e \approx 1.0$–1.5 MK. The observed loop oscillations occurred during a flare that began at 1998 July 14, 12:55 UT and are most prominent during the first 20 minutes. The oscillating loops connect the penumbra of the leading sunspot to the flare site in the trailing portion. We identified five oscillating loops with an average length of $L = 130{,}000 \pm 30{,}000$ km. The transverse amplitude of the oscillations is $A = 4100 \pm 1300$ km, and the mean period is $T = 280 \pm 30$ s. The oscillation mode appears to be a standing wave mode (with fixed nodes at the footpoints). We investigate different MHD wave modes and find that the *fast kink mode* with a period $\tau = 205(L/10^{10}\ \mathrm{cm})(n_e/10^9\ \mathrm{cm}^{-3})^{1/2}(B/10\ \mathrm{G})^{-1}$ s provides the best agreement with the observed period. We propose that the onset of loop oscillations in distant locations is triggered by a signal or disturbance that propagates from the central flare site with a radial speed of ≈ 700 km s^{-1}. Because the observed loop oscillation periods are comparable to photospheric 5 minute oscillations, a resonant coupling between the two systems is possible. We further find evidence for global extreme-UV dimming in the entire active region possibly associated with a coronal mass ejection.

Subject headings: Sun: corona — Sun: flares — Sun: oscillations — Sun: UV radiation

1. INTRODUCTION

In this paper, we report the first detection of *spatial displacement oscillations* of coronal loops, observed for the first time as a result of the high spatial resolution of the *Transition Region and Coronal Explorer* (*TRACE*) telescope. Such oscillations of coronal loops or flux tubes can provide information on resonance conditions, limit cycles of nonlinear systems, or periodic drivers. The search for oscillations in coronal loops is also strongly motivated by coronal heating theories that involve wave interactions, e.g., resonant heating by dissipative Alfvén waves (Steinolfson & Davila 1993). A number of oscillatory phenomena are known from inside the Sun (helioseismology, 5 minute oscillations) and near the solar surface (running penumbral waves, Moreton waves, Sun quakes), but there is no observational evidence yet whether and how these oscillatory phenomena might couple to magnetic structures in the corona. There are very few imaging observations that document oscillatory phenomena in the solar corona, while there is a larger number of indirect inferences based on quasi-periodic patterns observed in time profiles.

There are a number of previous reports on temporal oscillations in the solar corona in almost all wavelengths, with the majority in radio wavelengths (see review by Aschwanden 1987a). A compilation of these reports is provided in Table 1, ordered according to wavelength regime (hard X-ray, soft X-ray, UV/extreme-UV, optical, radio/mm/cm/dm/m/Dm). Table 1 summarizes the relevant literature references, instruments, observing methods, oscillation periods, and theoretical interpretations. The measured oscillation periods cover some 5 orders of magnitude ($T \approx 10^{-2}$ to 10^3s) and are likely to be associated with different physical oscillation mechanisms. Nevertheless, the majority of these oscillations have been attributed to global modes of MHD oscillations in coronal loops, while a subset of observations with less regular periodicities have been interpreted in terms of limit cycles of nonlinear wave-particle interactions in coronal loops. A few oscillations with periods near 5 minutes have been associated with a coupling mechanism to photospheric 5 minute oscillations. Although MHD oscillations provide a common mechanism to modulate radiation at different wavelengths, the diagnostic in each wavelength regime depends specifically on the dynamics of the plasma or trapped particles. Global MHD oscillations in the sausage mode (Roberts, Edwin, & Benz 1984) modulate loop cross sections and thus the density and emission measure of radiating plasma. The radiation from oscillating loops can be modulated (1) by the density of the emitting particles, leading to a density-squared response for incoherent emission mechanisms (e.g., free-free emission, atomic line emission, or bremsstrahlung) or (2) by pitch-angle modulation of trapped particles, leading to a density-proportional response for incoherent emission (e.g., gyrosynchrotron emission) or a nonlinear response for coherent emission mechanisms (e.g., loss-cone–driven or beam-driven radio emission). In contrast, global MHD oscillations in the kink mode do not change the loop density in first order and thus do not modulate the emitted radiation but are detectable as transverse displacements of spatial loop positions between fixed nodes.

Most previous reports on coronal loop oscillations are based on time-series analysis (labeled with *T* in Table 1). There are a few imaging observations of coronal loop oscillations (labeled with *I* in Table 1), mostly restricted to one-dimensional scans. Even those reports with two-dimensional imaging capabilities see only temporal oscillations of the total flux, and no spatial motion of the oscillating system has been detected, probably because of insufficient spatial resolution. The only reports of spatial motions with oscillatory characteristics are in recent *SOHO*

TABLE 1

OBSERVATIONS RELATED TO CORONAL LOOP OSCILLATIONS

Wavelength Regime[a]	Instrument Observatory	Method[b]	Oscillation Period (s)	Physical Interpretation[c]	References
HXR	Balloon	T	16	...	1
	OSO-5	T	10–100	...	2
	Hinotori	T	0.3	MHD	3
	SMM/HXRBS	T	8.2	...	4
	Venera	T	2–7	MHD	5
SXR	*SMM*/HXIS	I(2D)	>1440	MHD, p	6
	OSO-7	T	1.6	MHD, k	7
	GOES	T	1200	MHD, sl	8
	Yohkoh/SXT	T	9.6–61.6	MHD	9, 10
UV/EUV.....	SKYLAB	I(1D)	141	MHD, p	11
	SOHO/EIT	I(2D)	600–900	MHD, p	12
	TRACE	I(2D)	260–312	MHD, k+PPO	13
Optical	Sacramento Peak	T	43, 80, 300	MHD+PPO	14
	Hyderabad	T	0.5–2	MHD	15
	East Java	T	0.5–4	MHD	16
	Udaipur	T	180–300	PPO	17
Radio/mm	Kitt Peak	T	180	PPO	18
	Bordeaux	T	160–250	PPO	19
	Itapetinga	T	336	MHD+PPO	20
	Itapetinga	T	0.03	...	21
Radio/cm	Sagamore Hill	T	17, 23	...	22
	Itapetinga	T	2460	MHD	23
	Itapetinga	T	0.2–0.5, 1.5	MHD	3, 24, 25
	Westerbork	I(1D)	1.5	MHD	26
	Yunnan	T	0.18, 4	MHD	27
	Beijing	T	1.5, 40	MHD	28
	Nanjing	T	0.01–0.3		29
	Crimea	T	22–34	...	30
Radio/dm	Silver Spring	T	0.5	MHD, NLC	31
	Oslo	T	0.1–1.1	NLC	32, 33
	Zurich	T	0.1–5	NLC	34–42
	VLA, OVRO	I(2D)	8.8	MHD	43
	Yunnan	T	44–47	MHD, k	44
Radio/m	Kiel	T	0.2–1.2	...	45
	Trieste	T	1.7–3.1	MHD	46–48
	Utrecht	T	0.7–3.5	MHD	49–51
	Culgoora	T	2.5–4.3	MHD	52–53
	Nançay	I(1D),T	0.37, 1.7	MHD	54–55
	Nançay	I(1D),T	60	MHD	56
	Cranleigh	T	0.06–5	MHD, NLC	57
	Dwingeloo	T	0.2–5.5	...	58
	Izmiran	T	0.3–5	MHD	59
	Tremsdorf	T	44–60	MHD	60
	Tremsdorf	T	0.25–2	...	61
	Tremsdorf	T	1.0, 3.5	NLC	62, 63
	VLA,Trieste	I(2D)	9.8–14.2	MHD	64
	Nançay,ARTEMIS	I(1D)	180, 0.2	...	65
Radio/Dm	Kingston	T	4.0	MHD	66
	Gauribidanur	I(1D)	2–5	NLC	67

[a] Wavelength regimes in radio: Dm = Decametric (3–30 MHz), m = metric (30–300 MHz), dm = decimetric (0.3–3 GHz), cm = centimetric (3–30 GHz), mm = millimeter (30–300 GHz)

[b] Method: I = Images (1D = one-dimensional scans, 2D = two-dimensional images), T = time series analysis

[c] Physical interpretation: MHD = MHD wave modes (s = sausage mode, k = kink mode, sl = slow mode, p = propagating Alfvén waves), NLC = nonlinear limit cycle, PPO = photospheric (5 minute) *p*-mode oscillations

REFERENCES.—(1) Parks & Winckler 1969; (2) Lipa 1978; (3) Takakura et al. 1983; (4) Kiplinger et al. 1983; (5) Desai et al. 1987; (6) Harrison 1987; (7) Thomas, Neupert, & Thompson 1987; (8) Svestka 1994; (9) McKenzie 1997; (10) McKenzie & Mullan 1997; (11) Antonucci, Gabriel, & Patchett 1984; (12) DeForest & Gurman 1998; (13) this work; (14) Koutchmy et al. 1983; (15) Pasachoff & Landman 1984; (16) Pasachoff & Ladd 1987; (17) Jain & Tripathy 1998; (18) Simon & Shimabukuro 1971; (19) Bocchia & Puomeyrol 1974; (20) Strauss et al. 1980; (21) Costa & Kaufmann 1986; (22) Janssens & White 1969; (23) Kaufmann 1972; (24) Zodi, Kaufmann, & Zirin 1984; (25) Correia & Kaufmann 1987; (26) Kattenberg & Kuperus 1983; (27) Fu et al. 1990; (28) Qin & Guang-Li 1994; (29) Qin, Li, & Fu 1996; (30) Baranov & Tsvetkov 1994; (31) Gotwols 1972; (32) Elgarøy & Sveen 1973; (33) Elgarøy 1980; (34) Bernold 1980; (35) Wiehl, Benz, & Aschwanden 1985; (36) Aschwanden 1986; (37) Aschwanden 1987b; (38) Aschwanden et al. 1993; (39) Aschwanden, Benz, & Montello 1994a; (40) Aschwanden et al. 1994b; (41) Aschwanden, Dennis, & Benz 1998; (42) Kurths, Benz, & Aschwanden 1991; (43) Aschwanden, Bastian, & Gary 1992; (44) Wang & Xie 1997; (45) Dröge 1967; (46) Abrami 1970; (47) Abrami 1972; (48) Abrami & Koren 1978; (49) Rosenberg 1970; (50) Rosenberg 1972; (51) DeGroot 1970; (52) McLean et al. 1971; (53) McLean & Sheridan 1973; (54) Pick & Trottet 1978; (55) Trottet et al. 1981; (56) Trottet, Pick, & Heyvaerts 1979; (57) Tapping 1978; (58) Slottje 1981; (59) Zaitsev, Stepanov, & Chernov 1984; (60) Aurass & Mann 1987; (61) Aurass et al. 1987; (62) Kurths & Herzel 1986; (63) Kurths & Karlicky 1989; (64) Zlobec et al. 1992; (65) Chernov et al. 1998; (66) Achong 1974; (67) Sastry, Krishan, & Subramanian 1981.

171 Å observations and are interpreted in terms of quasi-periodic wave trains in polar plumes (DeForest & Gurman 1998). Also notable is a systematic search for oscillating loops in *Yohkoh*/SXT images revealing marginal oscillations in brightness with amplitudes of $\approx 1\%$ and periods of 9.6–61.6 s (McKenzie 1997; McKenzie & Mullan 1997). Nevertheless, the physical mechanisms behind oscillatory phenomena in the solar corona, which cover a wide range of wavelengths and periods, are still virtually unidentified, mainly because of no, or poor, spatial resolution and insufficient time cadence. The unprecedented spatial resolution and high time cadence of the *TRACE* telescope, of $\lesssim 1''$ (in extreme-UV [EUV]) has allowed us to see *spatial displacement oscillations* in loops for the first time. The loop oscillations discussed here were observed during a flare that occurred in the southeast quadrant of the solar disk on 1998 July 14. In § 2 we describe the data analysis of the observed loop oscillations and the role of the flare. In § 3 we interpret this phenomenon in terms of physical wave modes. Flare-related global intensity variations are discussed in § 4. Conclusions are summarized in § 5.

2. DATA ANALYSIS

2.1. *Observations*

The *TRACE* spacecraft carries a 30 cm aperture telescope with four coatings for normal-incidence EUV and UV observations at wavelengths of 171 Å (Fe IX), 195 Å (Fe XII), 284 Å (Fe XV), 1216 Å (H I Lyα), 1550–1700 Å (continuum and C I, Fe II, C IV lines), and white light. Images are recorded on a 1024 × 1024 CCD detector with a pixel size of 0.″5 and a field of view of 8.′5 × 8.′5. *TRACE* was launched in 1998 April and has operated successfully since. For a technical description of the *TRACE* instrument see Tarbell et al. (1994) and Handy et al. (1999).

We analyze a sequence of *TRACE* 171 and 195 Å images of active region AR 8270 on 1998 July 14 during which a flare (*GOES* class M4.6) was reported with a start time around 12:55 UT. A sequence was taken, interleaving 171 and 195 Å exposures with an average cadence in each wavelength of 74 s in full resolution mode, i.e., 768 × 768 pixel images with a pixel size of 0.″5. We study the time interval from 12:00 through 14:15 UT, covering 1 hr before the flare and 1.3 hr of the postflare phase, containing 88 images in each wavelength with an almost constant cadence. The pointing of the image center, which is close to the flare location, is (−284″, −363″) from Sun disk center, i.e., in the southeast quadrant. The images have been co-aligned by cross-correlation to correct for solar rotation and spacecraft pointing jitter. They have also been despiked, and the readout pedestal of 86 DN (digital number) has been subtracted.

2.2. *The Development of the Flare*

We first describe briefly the development of the flare, as seen in the 171 Å bandpass of *TRACE*. In Figure 1 we show a single frame from the sequence: the first 171 Å image made after flare start, recorded at 12:55:16 UT with an exposure time of 16 s. This last long-exposure (and unsaturated) image before the explosive flare brightening displays the global dipolar magnetic structure of the active region. At flare start, some small-scale loops along a neutral line in the trailing region brighten up, straddling the locations marked with C_1, C_2, and C_3 in Figures 1 and 2. The EUV brightness saturates first near the location C_1, where a diagonal diffraction pattern (from the mesh that supports the entrance filter) becomes visible. Several loops are numbered: these will be referred to later in the article. The five oscillating loops are numbered (4, 6, 7, 8, 9) and outlined for quick identification. The geometric length of these loops is estimated by multiplying the projected footpoint separation by a factor of $\pi/2$, yielding lengths between $L = 90{,}000$ and $L = 160{,}000$ km (Table 2).

In Figure 2 we show three running difference images. In all panels, the centers of the diagonal diffraction patterns, which mark the four brightest flare kernels, are shown with cross symbols, and the diffraction spokes indicated by thin lines. As mentioned above, the brightness saturates first at C_1, and in the first difference image, made between the first flare image (12:55:16 UT) and the preceding (preflare) image (12:54:01 UT), a brightness change (black feature) is observable in a loop connecting C_1 with a position near the penumbra of the leading sunspot C_4. In the second difference image (Fig. 2, *middle panel*, 12:55:16/12:56:32 UT) there is a distinct change in the shape and brightness of this loop at C4, visible in the movie as a bright, kinked feature. This suggests that the loop, which exhibited flows before the flare, is closely connected to the site of flare triggering, at C1 or C4.

The second and third difference images indicate that the whole active region undergoes changes, presumably associated with the flare. The dominant features in the difference image are the diffraction spikes. They indicate changes in intensity and position of the flare kernels. But within the loop system, characteristic patterns of dark and light stripes also indicate global movements of loops, and the appearance of bright loop structures indicates an increase in intrinsic intensity. The oscillating loops are located within these moving loop groups, both to the north and to the south of the flare site, although the oscillations only become apparent in later difference images. A further significant feature of these first three difference images is that in consecutive frames, locations progressively farther from the flare site undergo changes (intrinsic brightenings or movement),

TABLE 2

BEST-FIT PARAMETERS OF LOOP OSCILLATIONS

Loop Number	Length L (Mm)	Amplitude A_1 (Mm)	Amplitude A_1/L	Period T (s)	Phase t_0/T	Number of Pulses
4	90	2.0 ± 0.2	0.022	258	0.79	2.1
6	120	4.6 ± 0.2	0.038	269 ± 6	0.67 ± 0.01	5.4
7	130	3.9 ± 0.4	0.030	320 ± 10	0.87 ± 0.07	2.8
8	150	4.4 ± 0.3	0.029	258 ± 10	0.68 ± 0.09	4.5
9	160	5.6 ± 0.1	0.035	278 ± 5	0.91 ± 0.01	2.4
Average	130 ± 30	4.1 ± 1.3	0.031 ± 0.006	276 ± 25	0.78 ± 0.10	3.4 ± 1.4

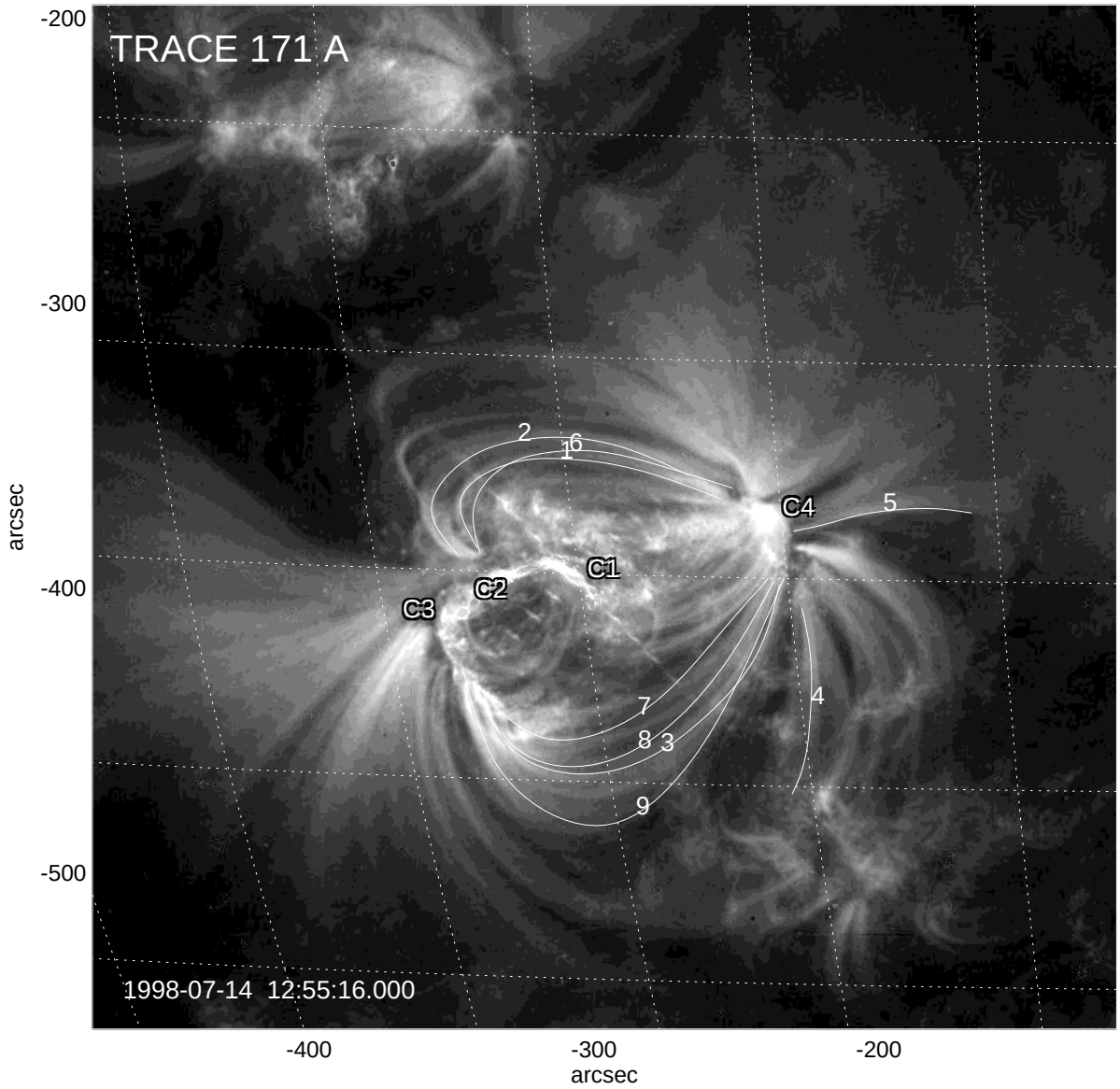

FIG. 1.—*TRACE* 171 Å image recorded at flare initiation, 1998 July 14, 12:55:16 UT, is shown with a logarithmic gray scale. This is also the last before brightness saturation occurs. The most prominent flare emission starts at location C_1 and progresses toward position C_3, straddling along the neutral line C_1-C_3. The diagonal pattern across the brightness maximum at C_1 is a diffraction effect of the telescope. The analyzed loops are outlined with thin lines. Loops 4 and 6–9 show pronounced oscillations.

which suggests a spreading of the response to the flare throughout the volume. We return to this later when considering the effect of the flare on the active region and the triggering of the loop oscillations.

2.3. *Loop Oscillations*

Displaying the sequence of *TRACE* images in a movie format (Schrijver et al. 1999) enables the eye to follow spatial oscillations of individual loops. Guided by this animation, we identified several oscillating loops during the 1998 July 14 flare, five of which are selected for detailed analysis.

An oscillating loop is recognizable as a dynamic feature with an oscillatory position sweeping over a more static background emission. The background often contains a number of other loops with similar orientation and similar brightness. It is difficult to separate the emission of the oscillatory loop from the background emission because the background emission often shows some time variability that adds confusion. A standard way to extract periodicities from time-varying data is to apply a Fourier transform method, but we were unable to do so here because of the small number of oscillation periods and sampling (of four data points per period) near the Nyquist frequency (i.e., two data points per period). Instead, we attempt to isolate the oscillating structures using the *running difference* of consecutive images. The images are first normalized in brightness to a common exposure time ($\Delta t_{\rm exp,\,0}$),

$$I^{\rm norm}(x, y, t) = [I(x, y, t) - I_0]\left[\frac{\Delta t_{\rm exp,0}}{\Delta t_{\rm exp}(t)}\right], \qquad (1)$$

after subtraction of the readout pedestal I_0. In order to separate transverse from longitudinal displacements we determine first the loop direction (near the loop top) and

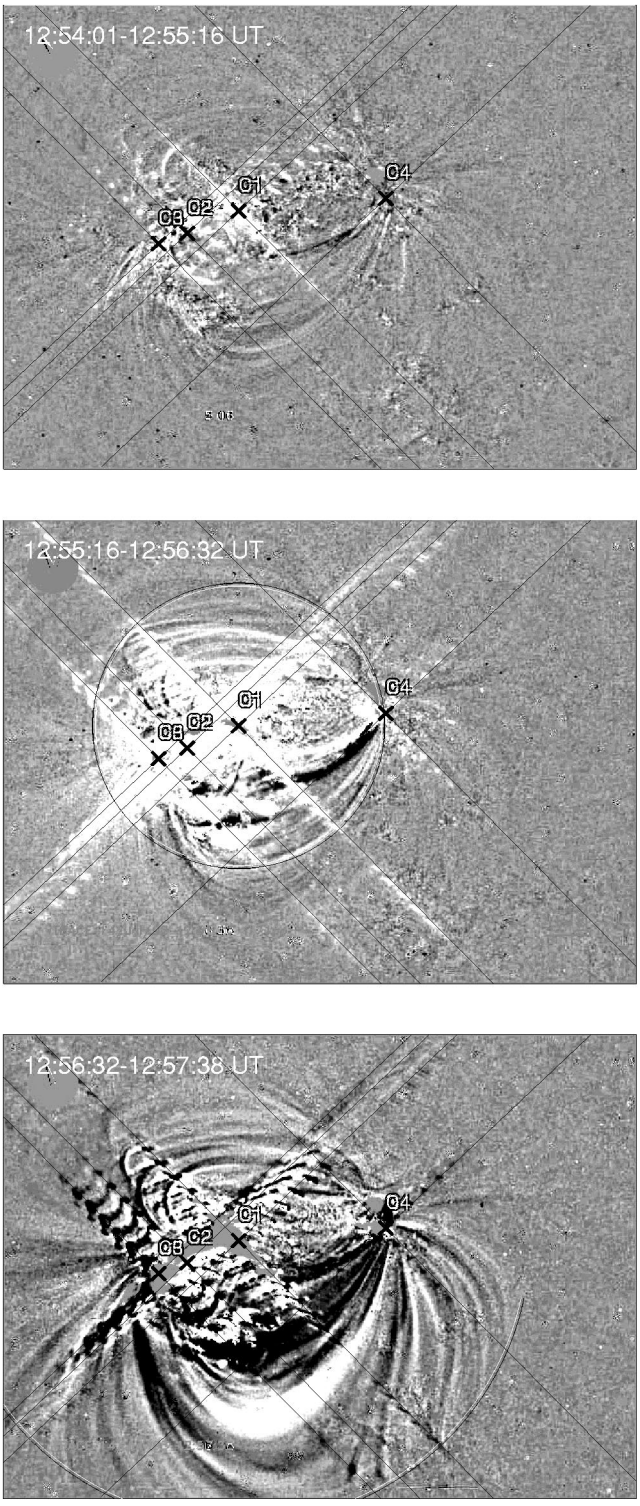

FIG. 2.—Sequence of 3 "running time difference" images is shown, extracted from *TRACE* 171 Å images with a mean cadence of ≈ 74 s, covering a slightly smaller field of view (640 × 480 pixels) than the full image shown in Fig. 1 (768 × 768 pixels). The difference images are created by subtracting the second time (indicated at the top of the panels) from the first time. White areas indicate therefore flux increase, while black areas indicate flux decrease. Note that a general EUV brightening of all loops occurs between 12:55:16 UT and 12:56:32 UT (*middle panel*). The dark shadows bordering white rims indicate spatial displacements of loops (*bottom panel*). The four most compact flare kernels are marked with C_1, C_2, C_3, and C_4, which are located at the centers of the diagonal diffraction patterns (*outlined with black thin lines*). The circles superposed in all three frames demarcate a propagating disturbance, assumed to start in C_1 at 12:55:08 UT and having a mean speed of $v = 700$ km s^{-1}.

interpolate data points in orthogonal directions $[a, b]$ to the loop. We indicate one such segment, of loop 6, in Figure 3 (*top row*). These extracted subimages from the entire time sequence of 88 co-aligned *TRACE* 171 Å images are then used to construct the running difference sequence, shown in Figure 3 (*third row*). In the representation in Figure 3, a brightness increase occurs in white, and a dimming in black. The oscillating loop is fainter than a brighter, but more static, loop that dominates the time sequence shown in Figure 3 (*second row*). However, after time-differencing, the static loop is largely subtracted out, while the spatial displacements of the oscillating loop dominate (Fig. 3, *third row*). The spatial oscillations $A(t)$ are now traced from the positions of the brightness maximum of the (slightly smoothed, with a boxcar of 10 pixels) difference flux $F(A, t + \Delta t) - F(A, t)$ (*diamonds*, in fourth and fifth rows of Fig. 3). The measured displacements $A(t)$ are shown in Figure 3 (*bottom row*), where we fit a sine function with four free parameters (A_0, A_1, T, t_0), viz.,

$$A(t_i) = A_0 + A_1 \sin\left[\frac{2\pi}{T}(t_i - t_0)\right]. \quad (2)$$

We find a best-fit period of $T = 275$ s. In order to corroborate the result we also trace the positions of the brightness *minimum* in the $(i - 1)$th image instead of the brightness maximum in the ith image, because both features occur for a spatial displacement. With this method we obtain a period of $T = 263$ s for the same loop (loop 6). We use the difference between the two methods as an estimate of the systematic error introduced by background time variability. Averaging the two values, we obtain a mean of $T = 269 \pm 6$ s. All errors given in Table 2 are estimated in the same way by averaging the best-fit parameters from both methods. To corroborate the significance of the measured oscillatory loop displacements, we performed reference measurements of loop 6 before the flare (12:00–12:55 UT) but obtained a null result.

In the same way we analyze four other oscillating loops. The measured oscillation amplitudes $A(t)$ of all five loops are shown in Figure 4, coregistered in time. The best-fit parameters are listed in Table 2. The number of detectable oscillations varies between 2.1 and 5.4 periods. The oscillation period is found to be similar for all five loops, with a mean of $T = 276 \pm 25$ s. Also, the relative phase is similar for all five loops, with a spread of only $\pm 10\%$. This synchronization within $\approx 20\%$ indicates that the oscillations are excited almost simultaneously, i.e., within ≈ 1 minute given the ≈ 5 minute period. The amplitude of the transverse oscillation is $A_1 = 4100 \pm 1300$ km, which is a fraction of $A_1/L = 3.1\% \pm 0.6\%$ of the loop length ($L = 130{,}000 \pm 30{,}000$ km). The corresponding velocity maximum of the oscillatory motion is found to be $v_{\rm osc} = 2\pi A_1/T = 90 \pm 30$ km s^{-1}.

By measuring the oscillation period at different locations along the loop one can, in principle, distinguish between standing wave modes and propagating wave modes. In our sample of oscillating loops, the oscillating amplitude can be traced over at least a half-loop length in two loops only (4 and 6), where we find some phase shift of the order of $\lesssim 20\%$ (along the loops). The resulting wave mode can therefore be considered as a standing wave with fixed nodes (at the footpoints) to first order, but a slight twist of the order of 0.2 turns could be responsible for the phase shift,

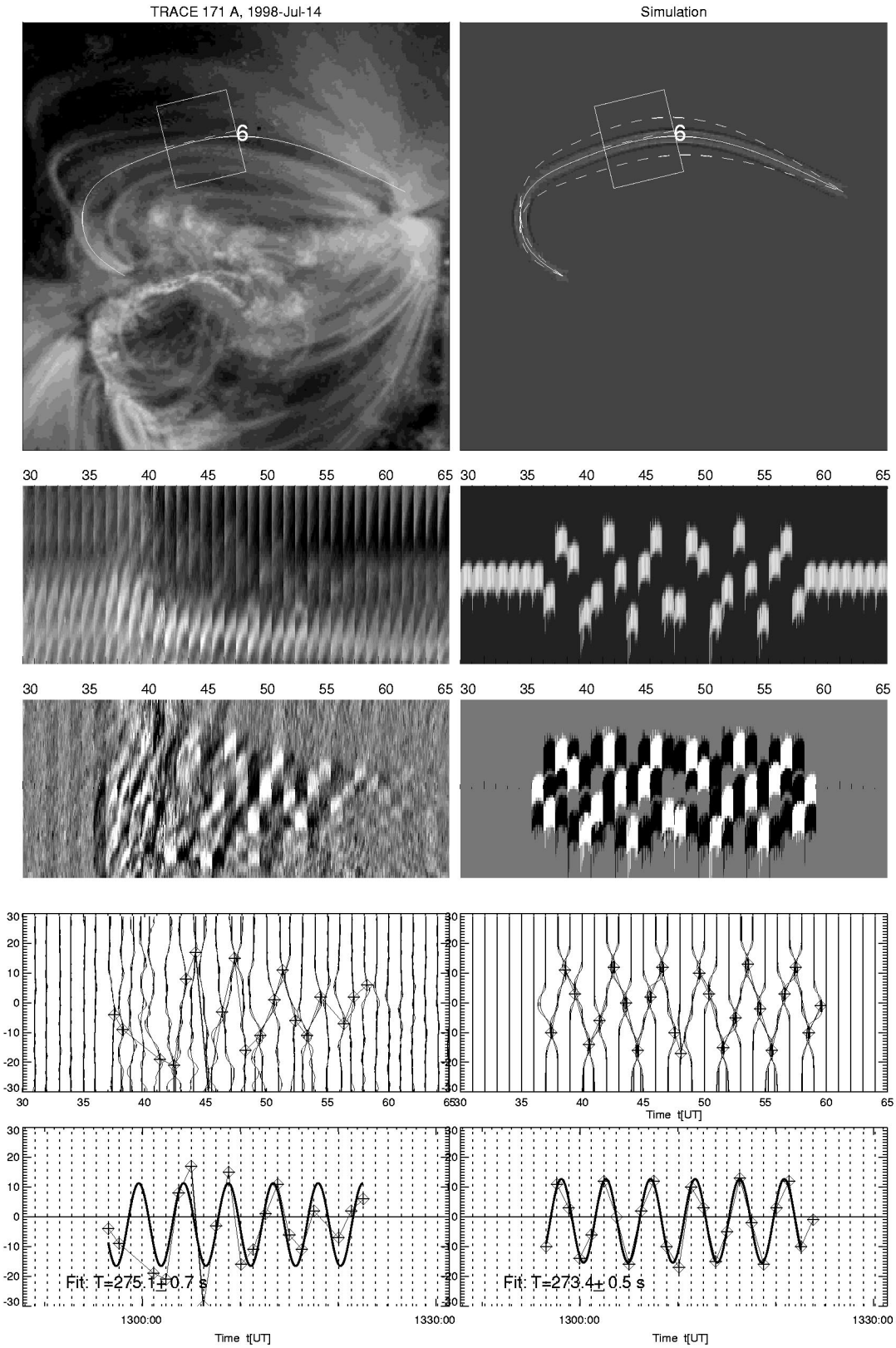

FIG. 3.—Measurement of oscillating loop amplitudes from difference images (*left column*) and a corresponding simulation (*right column*). The location of the analyzed loop (loop 6) is outlined with a thin white curve (*top row*), where a data slice is extracted perpendicular to the loop at the apex (*white box*, *top row*). The second row shows a time sequence of data slices (extracted within the same box as selected in the top row). Note that the oscillating loop has a weaker EUV flux than some adjacent static loops. In the third row we show a "running difference" of the time data slices, which filters out static loops and enhances the spatial variation of the oscillating loop. Note that each displacement causes a brightness increase in a difference image and at the same time a dimming at the previous position in the preceding difference image. The resulting pattern can easily be understood with the simulation shown in the right-hand panels. In the fourth row we show the average (and slightly smoothed) flux profile $f(y)$ of each slice. The amplitude of the spatial oscillation is measured from absolute maxima in these profiles $f(y)$ (*diamonds*, *fourth row*). Maxima below a threshold of 5 DN are ignored. These maximum positions are fitted with a sinusoidal function (*bottom row*).

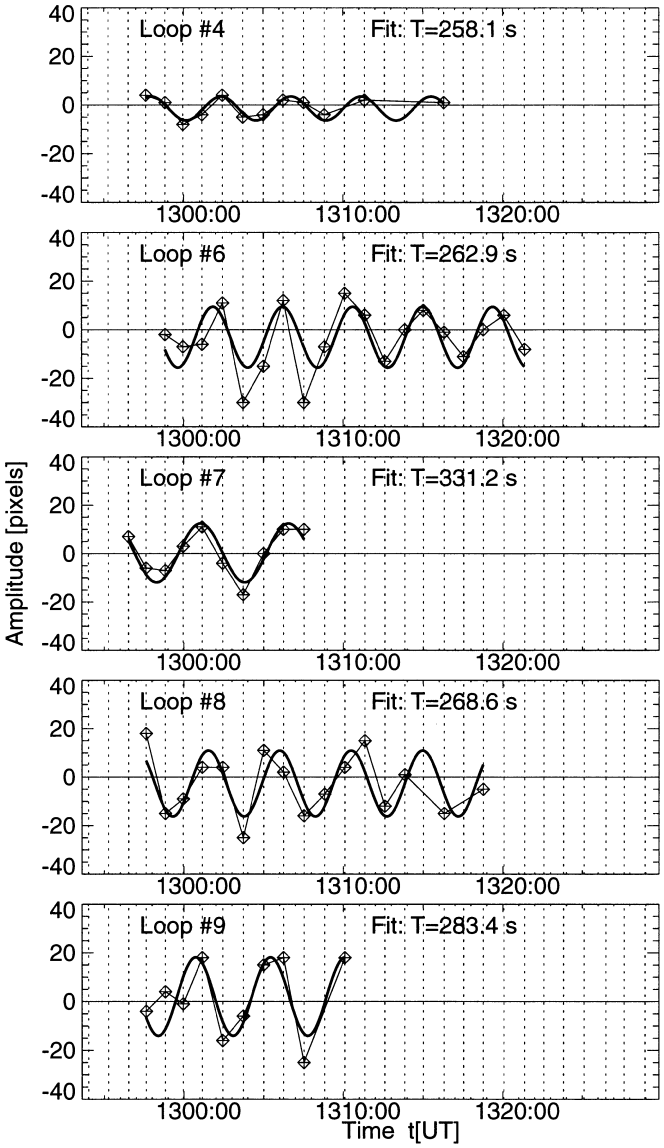

FIG. 4.—Spatial displacements of the analyzed five oscillating loops (4, 6–9) are shown (*diamonds*) and fitted with a sine function (*thick solid curve*) according to the same procedure as illustrated in Fig. 3. The spatial displacements are all measured in a perpendicular direction to the loops. Note that all periods and relative phases are similar, indicative of a common trigger.

perhaps caused by asymmetric excitation of the first oscillation amplitude due to propagation delays of the triggering disturbance. In the other three oscillating loops (7, 8, 9), confusion due to time variability of the background does not permit a reliable phase measurement of the oscillation amplitude along the loops.

2.4. *Coronal Loop Dynamics and the Excitation of the Oscillation*

We have established above that the five loops oscillate almost in phase, suggesting that the excitation of the oscillation is almost simultaneous throughout the loop group. Here we examine the possibility that the loops are set into oscillation by a traveling disturbance, generated by the flare or an associated process such as a coronal mass ejection (CME). Evidence for this traveling disturbance can be seen in the difference images of Figure 2.

In the first difference image the impulsive brightening of the flare kernels is confined to very compact regions, and the movements and intensity changes in the loops are small, typical of the changes seen between consecutive images in the preflare phase. In the second difference image, although the large diffraction spikes generated by the bright flare kernels dominate, there is also evidence of movement, and intensity increases in the surrounding loops. This is particularly visible in the loops to the north of flare kernel C1, where the maximum increase in counts is $\sim 15\%$ (this value is obtained from an average over 65×55 pixels with no subtraction of the diffuse "background" EUV emission and thus represents a lower limit of the intensity variations in individual loops). In the third difference image there is again movement and brightening in the loop system involving, this time, the field to the south. The brightest loop feature in this difference image reflects an increase in the counts of $\sim 50\%$. The loops to the southwest have also been moved outward, evidenced by the characteristic black and white stripes.

The involvement of ever more distant parts of the active region as time progresses suggests strongly that there is an outward-propagating disturbance or signal. This could be a pressure front, causing both loop displacements and localized density increases, leading to emission measure increases. Or possibly the "propagating" entity is the response of more and more distant parts of the loop system to changes in the magnetic field near the flare site (e.g., to flux removal, field reconfiguration, or current dissipation). This can be thought of as the propagation of an information signal. We discuss these possibilities further in § 4.

We can calculate a propagation speed for the disturbance. The circles on the panels in Figure 2 indicate the outermost positions at which significant changes (not including the diffraction spikes) are seen. Under the reasonable assumption that the disturbance is triggered by the flare, we have centered these curves on the brightest of the flare kernels, C1. From the positions of this disturbance in Figure 2, panels 2 and 3, we determine an outward propagation speed of ≈ 700 km s^{-1}. This will vary by perhaps 10%–30% depending on where we judge the center of the disturbance and the outer radii to be.

If there is indeed a propagating disturbance in the system, we should be able to predict the time at which it arrives at different positions in the active region and examine the loops for a response. We measure the loop positions of 5 bright loops (in 10 consecutive images) in the 13 minutes after the start of the flare in EUV. We do this by marking seven loop positions between the footpoints in an enlarged *TRACE* image display and interpolate the marked loop positions with a cubic spline fit. The superposed (coaligned) loop projections are shown in Figure 5 (*left column*). The positions of the five selected loops are also indicated in Figure 1 (numbered from 1 to 5). It is instructive to visualize the transverse displacements of the loops near the loop tops, which is shown in Figure 5 (*right column*) in the north-south direction for loops 1, 2, 3, and 5 and in east-west direction for loop 4. The series of 10 analyzed *TRACE* images (numbered 0–9 in Fig. 5, *right*) starts at the last preflare image at 12:54:01 UT and steps in increments of $\Delta t \approx 74$ s.

Using the propagation characteristics already determined, i.e., radial propagation with a projected speed of $v \approx 700$ km s^{-1}, starting from C_1 at 12:55:16 UT, we

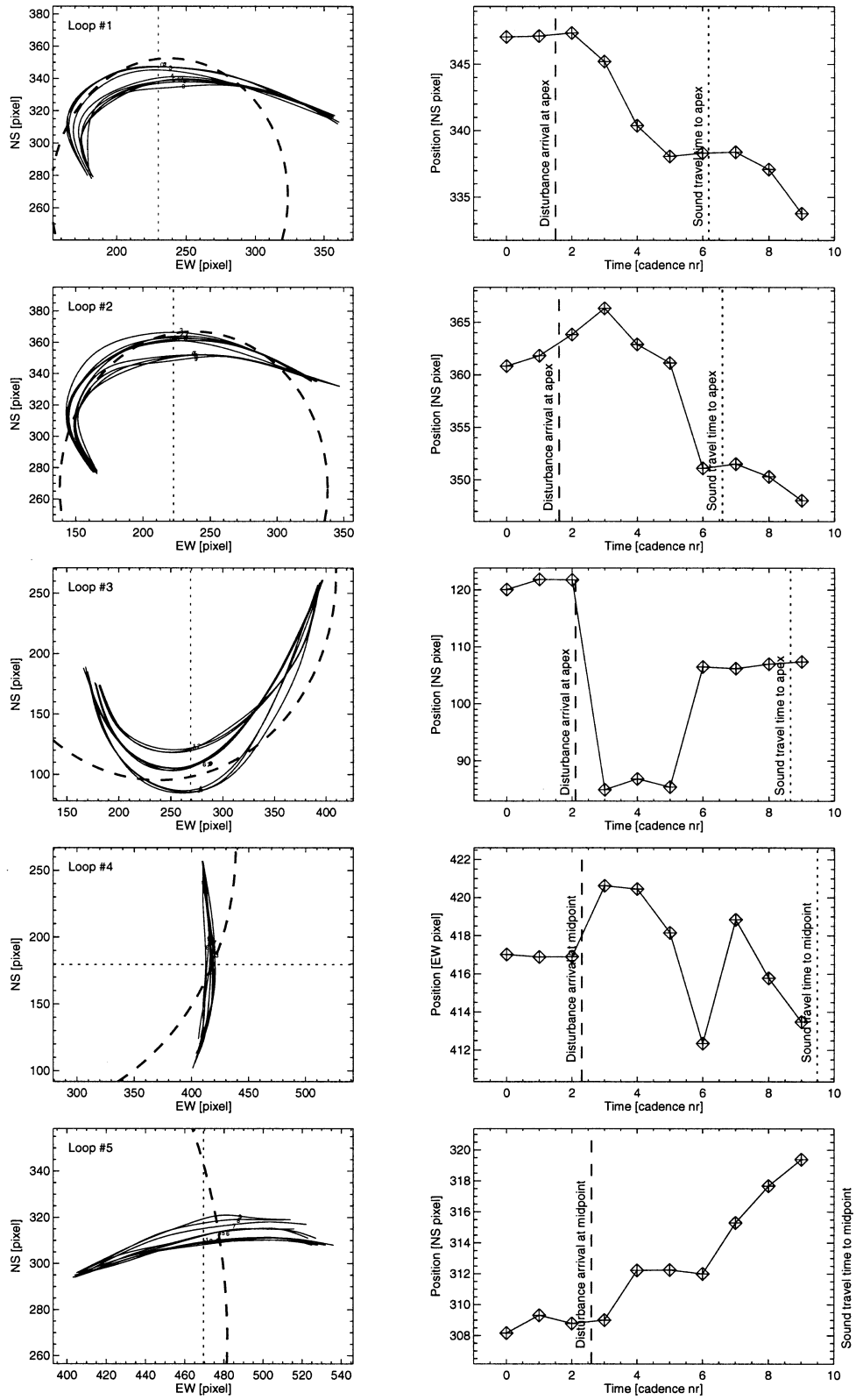

FIG. 5.—Spatial displacements of loops 1–5 are shown (*left panels*) during flare start. The time at which the propagating disturbance (*dashed circle*) passes the apex or midpoint of the loop section is marked with a dashed line. Note that the direction of propagation is almost perpendicular to loops 1–3, oblique to loop 4, and parallel to loop 5. All loops show a rapid displacement after the predicted arrival time. The transverse loop displacement at the loop apex is measured in north-south or east-west direction (*dotted line, left panels*) and is shown as function of time (*right panels*). The time axis (*right panels*) refers to the cadence number of 10 subsequent images, starting at 12:54:01 UT and increasing in increments of ≈ 74 s. The approximate sound travel time from loop footpoint to the apex/midpoint of the loop section is shown with a dotted line (*right panels*).

predict that the disturbance would arrive at the apices of loops 1, 2, and 3 after $\Delta t \approx 103$, 110, and 147 s, respectively, and at the approximate center of the visible parts of loops 4 and 5 after $\Delta t \approx 162$ and 184 s. These predicted arrival times are shown by a dashed line in the displacement versus time plot for each loop (Fig. 5, *right-hand column*). It can be seen clearly that the movement of each loop is consistent with a prompt response to the passage of the proposed radially propagating disturbance, sometimes by a rapid transverse displacement in the downstream direction with subsequent retraction in upstream direction (loops 2, 3, and 4), or by a more complex response pattern. For loops 1, 2, and 3, the propagation direction is almost perpendicular to the loop (near the loop top), while it is oblique for loop 4 and parallel for loop 5. Loop 4 starts to oscillate, while the displacement of the other loops appears to be strongly damped. We can only see a small segment of loop 5, which may be part of an open or a closed field line. This loop sways only in one direction (to the north), and our supposed propagation direction is parallel to the field line.

The spatial scale of loop displacements is on the order of 10 *TRACE* pixels ($\approx$3500 km) for most cases (loops 1, 2, 4, and 5) but can be as large as $\approx$30 pixels ($\approx$10,000 km), e.g., for loop 3. These 5 loops have a typical width of $w \approx 1000$ km and a length of $L \gtrsim 100{,}000$ km. Note that the crossing time of the disturbance across a loop diameter is only $\approx$1 s, while the travel time from loop footpoint to loop apex is about 150 s, comparable with the *TRACE* cadence (74 s).

2.5. *Temperature Diagnostics*

Investigating other temperature passband filters from *TRACE* and *Yohkoh*, we can constrain the temperature range of the oscillating loops. The temperature response of the 171 Å filter of *TRACE* peaks at $T_e \approx 1.0$ MK. We produced a movie from the *TRACE* 195 Å images with identical cadence and time coverage and repeated the same analysis procedure with identical fields as the 171 Å data. During the first 20 minutes of the postflare phase, an oscillation similar to that seen at 171 Å is detectable in difference images of the 195 Å filter. The brightness contrast is much weaker, however, and consequently the oscillation amplitude and period are more difficult to quantify. This is consistent with a temperature range of $T_e \approx 1.0$–1.5 MK for the oscillating loops, which overlaps only marginally with the response function of the 195 Å bandpass.

Yohkoh/SXT data are sensitive to a temperature of $T_e \gtrsim 2$ MK. *Yohkoh*/SXT was operated in flare mode during the postflare phase, from 12:33 to 12:57 UT. An SXT Al.1 filter image taken at 13:04:57 UT is shown in Figure 6, overlaid on a simultaneous *TRACE* image recorded at 13:05:00 UT (An empirical correction of 10″ to the north has been applied to the *TRACE* image in the co-alignment with the *Yohkoh*/SXT image.) The data show that the heated flare plasma is entirely confined to the arcade of flare loops that straddles the central neutral line (C_1-C_3 in Fig. 1). No detectable coronal plasma seems to be heated to soft X-ray

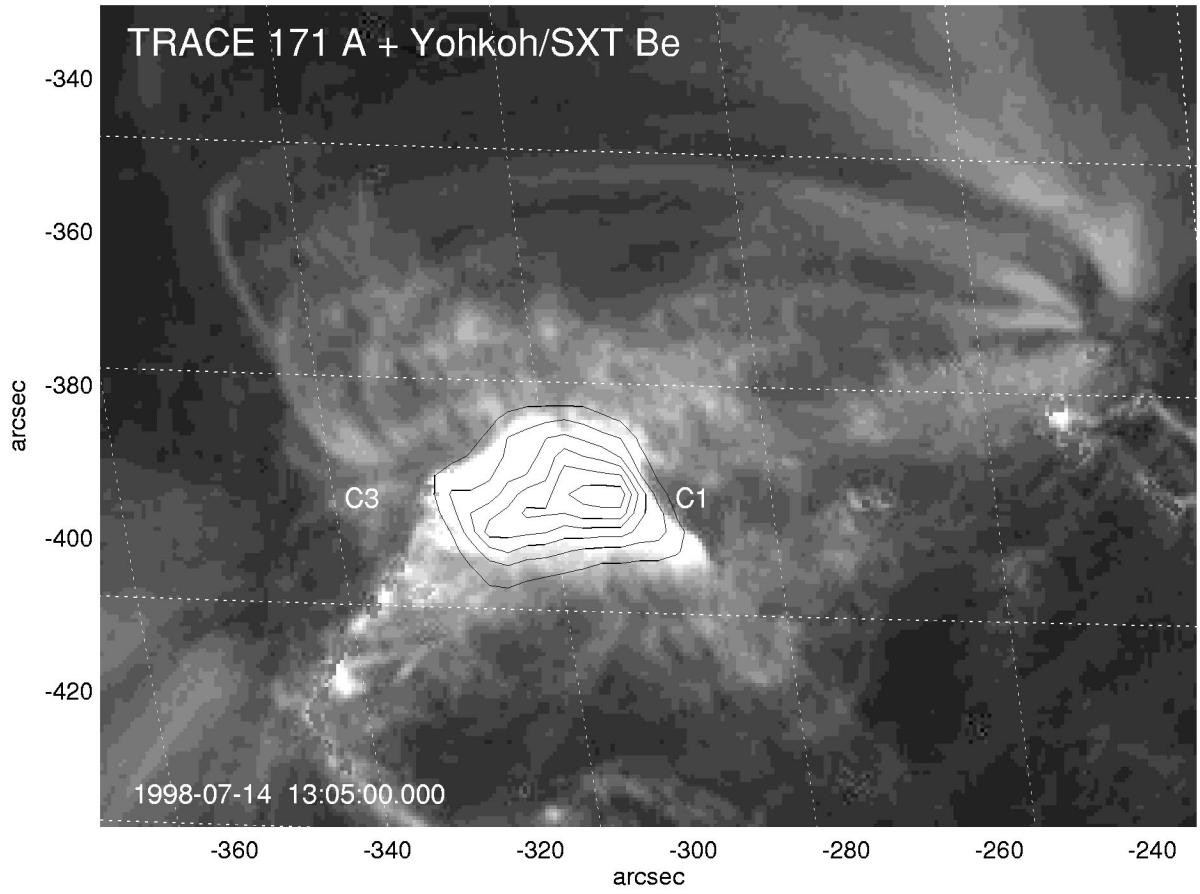

FIG. 6.—*TRACE* 171 Å image of 1998 July 14, 13:05:00 UT (*gray scale*), overlaid with contours of simultaneous *Yohkoh*/SXT Al.1 image, 13:04:57 UT, about 10 minutes after flare start. The contour levels range from 10% to 90% of the peak SXT brightness. Note that the soft X-ray flare plasma is entirely confined to the arcade that is also brightest in the EUV located above the neutral line C_1-C_3.

temperatures at the location of the oscillating loops. The *Yohkoh*/SXT data imply, therefore, that the flare did not heat the oscillating loops or the neighboring loops significantly. The 195–171 Å flux ratio R in these loops increases not more than 10% during the first few time frames and corresponds to an even smaller percentage change in loop temperature T_e (because it is where the theoretical filter ratio R has the steepest gradient dR/dT_e). Therefore, brightness variations due to temperature changes can be largely ruled out.

3. DISCUSSION OF OSCILLATION MODES

We now investigate different physical mechanisms that have been proposed to explain oscillations of coronal plasma loops and compare their theoretical oscillation periods with our observed data. For numerical estimates of oscillation periods we use the mean observed loop size (i.e., loop length $L \approx 130{,}000$ km) and the mean electron temperature of the 171 Å passband ($T_e \approx 1.0$ MK). For other physical parameters we substitute mean values that have been measured from the statistics of 30 similar loops in a comparable active region, analyzed from *SOHO*/EUV Imaging Telescope (EIT) at the same wavelength of 171 Å (Aschwanden et al. 1999). The observed loop lengths suggest a typical altitude of $h = L/\pi \approx 40{,}000$ km for the loop tops. We calculate the physical parameters obtained from the *SOHO*/EIT study for this height h, i.e., an electron density $n_e = 1.0 \times 10^9$ cm^{-3} (with a variation by a factor of 1.3) and a magnetic field $B = 20$ G (within a variation by a factor of 3). The average loop width (measured in *SOHO*/EIT images) was found to be $a \approx 3500$ km. This value may be biased by the spatial resolution of the instrument and could be substantially lower for *TRACE* observations.

3.1. *Standing Fast MHD Waves*

In a magnetically structured atmosphere, plasma is confined along a magnetic field line with some cross section. Slender, overdense coronal flux tubes can be approximated with a cylindrical geometry. For pressure balance across the surface boundary and neglecting gravitational effects, resonance conditions have been computed for free modes of standing MHD waves, where the homogeneously filled flux-tube volume oscillates as a whole (also called body waves), while the surface has a nonvanishing amplitude only near the flux-tube boundary (surface waves). The free oscillation modes have been subdivided into symmetric (sausage-type) and asymmetric (kink-type) modes. These free modes have a phase speed of $\omega/k \gtrsim v_A$ and are therefore called *fast MHD waves*. The sound speed is generally sub-Alfvénic ($c_0 < v_A$) under coronal conditions.

We examine first the *fast sausage mode*, since it has been previously employed in the interpretation of coronal loop oscillations detected in radio. Here, however, we can rule out the sausage mode for two reasons: (1) the observed spatial displacements (i.e., asymmetric mode) are inconsistent with the symmetric sausage mode, and (2) the oscillation period observed here is much longer than that of the sausage mode. The oscillation period has been calculated (in cgs units) to be (Wentzel 1979; Edwin & Roberts 1983; Roberts et al. 1984)

$$\tau_{\rm sausage}^{\rm fast} = \frac{2\pi a}{c_k} = 4\pi^{3/2} a \left(\frac{\rho_0 + \rho_e}{B_0^2 + B_e^2}\right)^{1/2} \approx 6.4 \, \frac{a_8 \sqrt{n_9}}{B_{10}} \, \text{s} \, , \quad (3)$$

with c_k the phase speed, $\rho = n_i m_i$ the ion mass density, and a the radius of the flux tube; the subscript indices 0 and e refer to inside and outside of the loop. The approximation on the right-hand side is for $B_0 \approx B_e$, $\rho_e \ll \rho_0$, and $n_i \approx n_e$, specified in units of $a_8 = a/10^8$ cm, $n_9 = n_e/10^9$ cm^{-3}, and $B_{10} = B/10$ G. For typical parameters of EUV loops we obtain a mean period of $\tau_{\rm sausage}^{\rm fast} \approx 11$ s, with a variation by a factor of 4, i.e., in the range of $\tau_{\rm sausage}^{\rm fast} \approx 3$–44 s. The fast sausage mode period is thus much shorter than the observed period of $T = 276$ s.

For the *fast kink mode*, which corresponds to asymmetric lateral displacements, the oscillation period depends also on the number of nodes $j - 1$ along the loop. The period was calculated to be (Edwin & Roberts 1983; Roberts et al. 1984)

$$\tau_{\rm kink}^{\rm fast} = \frac{2L}{jc_k} = 4\pi^{1/2} \frac{L}{j} \left(\frac{\rho_0 + \rho_e}{B_0^2 + B_e^2}\right)^{1/2} \approx 205 \, \frac{L_{10} \sqrt{n_9}}{B_{10}} \, \text{s} \, , \quad (4)$$

where we again assume $\rho_0 \ll \rho_e$, $B_0 \approx B_e$, and $j = 1$. Thus we find a mean period of $\tau_{\rm kink}^{\rm fast} \approx 123$ s, with a variation by a factor of 4, i.e., in the range of $\tau_{\rm kink}^{\rm fast} \approx 0.5$–7.8 minutes. The fast kink mode seems to be a strong candidate for the interpretation of the observed loop oscillation, not only because it produces compatible periods, but also because the asymmetric lateral displacements of the kink mode are consistent with the observed dynamic features. However, the observed periods do not vary with loop length in the expected manner. The periods measured in the five chosen loops agree to within $\approx 10\%$, but the loop lengths vary by $\approx 25\%$, and the longest loops do not have the longest period: see, for example, loops 4 and 7. Of course, n_e and B_0 will vary from loop to loop, but we do not see an obvious reason why their variation should compensate in such a way to keep the fast kink mode period constant. This may suggest another driver with a preference for cycles clustered around the observed 4.6 minute period, perhaps because it is close to the maximum power of photospheric oscillations. We discuss this further in § 3.4. Alternatively, Cargill, Chen, & Garren (1994) found periods of current-carrying loop oscillations that are almost insensitive to the loop length.

The fast kink mode was previously proposed to explain coronal oscillations in optical wavelengths (Roberts et al. 1984), e.g., to explain the periods ($\tau = 43$, 80, and 300 s) of coronal oscillations observed by Koutchmy, Zhugzhda, & Locans (1983), the 5.6 minute oscillation of radio sources observed by Strauss, Kaufmann, & Opher (1980), and oscillations in prominence fine structure (Joarder, Nakariakov, & Roberts 1997). The derived coronal magnetic fields in those two cases were $B = 15$ and $B = 44$ G (Roberts et al. 1984). The kink instability was also applied to model geometric changes of a coronal loop observed in He II (Cheng 1977).

3.2. *Standing Slow MHD Waves*

Investigating the dispersion relation of phase speeds under coronal conditions (where the Alfvén velocity is larger than the sound speed c_0), solutions of slow MHD waves (on an acoustic timescale) have also been identified as a separate branch of solutions of the dispersion relation. Standing slow MHD waves have the following periods, which are almost identical for both sausage-type and kink-

type modes, (Edwin & Roberts 1983; Roberts et al. 1984),

$$\tau_{\rm slow} = \frac{2L}{jc_T} = \frac{2L}{jc_0}\left[1 + \left(\frac{c_0}{v_{\rm A}}\right)^2\right]^{1/2} \approx 1300\,\frac{L_{10}}{\sqrt{T_6}}\ {\rm s}\ , \quad (5)$$

with $c_T = c_0\, v_a/(c_0^2 + v_{\rm A}^2)^{1/2}$ and the sound speed $c_0 \approx 1.5 \times 10^4 T_e^{1/2}$. The approximation on the right-hand side is made for coronal conditions $c_0 \ll v_{\rm A}$ and for node $j = 1$. Temperature is in units of $T_6 = T_e/10^6$ K. For typical EUV loops we estimate a mean period of $\tau_{\rm slow} \approx 1300$ s or about 20 minutes. Because the period depends only on the loop length L in first order, which is known with an accuracy of $\approx 10\%$ here, the predicted slow mode period covers a relatively narrow range, i.e., $\tau_{\rm slow} = 20 \pm 2$ minutes. They are clearly inconsistent with the observed period of $T = 276$ s, unless higher order nodes ($j \approx 4$) are invoked that are inconsistent with the observations.

3.3. *Propagating MHD Waves*

If a disturbance is generated impulsively at one end of a loop, propagating MHD waves will result rather than standing modes. Such waves arise in a coronal loop especially if the motions have insufficient time to reflect from the far end of the loop or propagate into open field regions. Roberts et al. (1984) characterized the dynamic behavior of such impulsively generated fast waves by three phases: (1) a periodic phase starting at height h at time $t_1 = h/v_{Ae}$ and ending at time $t_2 = h/v_{\rm A}$ when high-frequency information arrives, (2) a quasi-periodic phase where wave amplitudes increase, and (3) a decay phase after $t_3 = h/c_{\rm gmin}$ when the last information with minimum group velocity $c_{\rm gmin}$ arrived. The characteristic period in the periodic and quasi-periodic phase was calculated by Roberts et al. (1984) in the low β-limit to be

$$\tau_{\rm prop} = \frac{2\pi a}{j_{0,1}\, v_{\rm A}}\left(1 - \frac{\rho_e}{\rho_0}\right)^{1/2} \approx 3.8\left(\frac{a_8\sqrt{n_9}}{B_{10}}\right)\ {\rm s}\ , \quad (6)$$

where $j_{0,1} \approx 2.4$ is the first zero of the Bessel function J_0. (For numerical simulations see Murawski, Aschwanden, & Smith 1998 and references therein.) This MHD period of propagating waves is a factor of 0.6 shorter than that of a standing MHD wave in the fast sausage mode (eq. [4]).

If we apply this period of propagating MHD waves to typical EUV loops, for which the Alfvén velocity at the loop top is $v_{\rm A} = B_0/(4\pi n_i m_i)^{1/2} \approx 1000$ km s^{-1}, we estimate $\tau_{\rm prop} \approx 6.7$ s (within a factor of 3.4) or within a range of $\tau_{\rm prop} \approx 2$–22 s. The duration of the periodic oscillation phase is expected to last $t_2 = h/v_{\rm A} = 190$ s at the loop top. Both the produced periods and the total duration of the oscillatory phase are too short to explain the observed loop oscillations.

3.4. *Photospheric 5 Minute Oscillations*

The measured loop period of $T \approx 4.6$ minutes lies within the range of frequencies (2.5–4.5 mHz, i.e., $\tau = 220$–400 s) where most of the power is found in the photospheric 5 minute oscillations. This is an interesting coincidence. Although the detected loop oscillations occur near the tops of large loops, at an estimated height of $h = 40{,}000$ km (if the loop geometry is approximated by a semicircle), a connection with photospheric 5 minute p-mode oscillations (Leighton, Noyes, & Simon 1962) cannot be ruled out. Photospheric 5 minute oscillations are standing acoustic waves trapped in a resonant cavity in and below the photosphere (e.g., Deubner & Gough 1984). Although the 5 minute oscillations are trapped inside the photosphere, while the overlying transition region acts like a reflector, the loops are rooted in the photosphere, and there will always be some leakage from the resonant cavity. Although no signature of the photospheric 5 minute oscillation is normally seen in coronal loops, oscillatory motion at the photospheric footpoints of coronal loops (Berghmans & DeBruyne 1995) could amplify coronal oscillations (generated by an entirely different process) if there is frequency matching between the photospheric oscillation and a coronal eigenmode. The observed strong loop oscillations could be the result of additional energy input to flare-triggered oscillations input just such a resonance.

From Figures 1 and 3 it can be seen that the oscillating loops are connected with the leading sunspot in the west side of the active region, either with the umbra or the penumbra or close to the penumbra. Chromospheric oscillations in sunspots have greater power at periods in the range 140–200 s for different spots, known as *umbral flashes*, having associated oscillations, (for a review see, e.g., Lites 1992). We would be hard pressed to detect oscillations of this period in our data, given the 74 s cadence with which we observe. However, a 5 minute period was also seen in spot penumbrae at reduced amplitude, indicating that the penumbra consists of individual flux tubes rather than having a monolithic structure (Thomas 1981; Foukal 1990, p. 373). So even if the loop is rooted in an umbral or penumbral region, the 5 minute oscillation could couple to and amplify an eigenmode of the coronal loop.

3.5. *Distribution of Oscillation Frequencies and the Probability of Coupling with the 5 Minute Oscillations*

In previous sections we discussed the oscillation periods of MHD waves under coronal conditions on the basis of assumed (reasonable) physical parameters. Now, using statistical parameters obtained from an analysis of 30 similar loops using *SOHO*/EIT, also in the 171 Å filter (Aschwanden et al. 1999; § 4), we are in a position to calculate the likely distribution of oscillation periods in a loop group. Furthermore, this gives us the means by which to estimate how many loops could be in resonance with a 5 minute photospheric driver.

The parameters obtained in the *SOHO*/EIT study are electron density at coronal footpoints $n_{e,0} = 2.0 \pm 0.6 \times 10^9$ cm^{-3}, electron density scale height $\lambda = 55 \pm 10 \times 10^8$ cm, loop height $h_{\rm loop} = 1.3 \pm 0.6 \times 10^{10}$ cm, loop radius $a = w/2 = (3.6 \pm 0.40) \times 10^8$ cm, loop temperature $T_e = 1.2 \pm 0.1 10^6$ K, and magnetic field at footpoint $B_0 = 10^{1.8 \pm 0.5}$ G, magnetic dipole depth $h_D \approx 7.5 \times 10^9$ cm^{-3}. From these parameters we define the density at the loop top $n_e^{\rm top}$ by

$$n_e^{\rm top} = n_e(h = h_{\rm loop}) = n_{e,0}\,\exp\left(\frac{-h_{\rm loop}}{\lambda}\right) \quad (7)$$

and the magnetic field at the loop top $B^{\rm top}$ from the dipole model

$$B^{\rm top} = B(h = h_{\rm loop}) = B_0\left[1 + \left(\frac{h_{\rm loop}}{h_D}\right)\right]^{-3}\ . \quad (8)$$

We calculate now the probability of the various MHD oscillation periods given in equations (4)–(7) by generating normal distributions for each parameter a, L, $n_e^{\rm top}$, and $B^{\rm top}$,

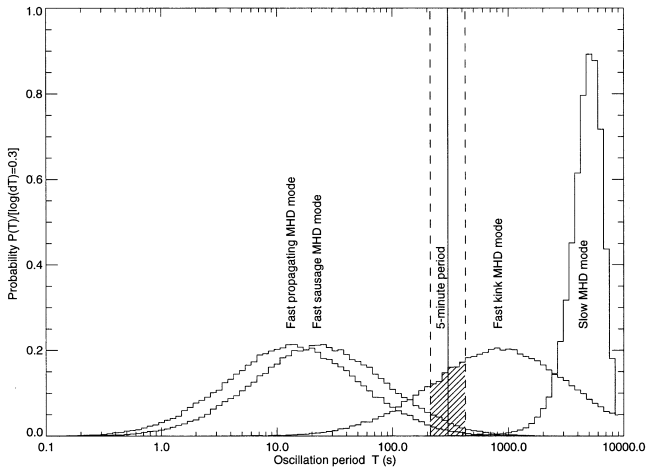

FIG. 7.—Probability distributions of four different MHD periods calculated for densities, magnetic fields, and altitudes that are typical for EUV loops observed in the temperature range of $T_e = 1.0$–1.5 MK (e.g., with *TRACE* or *SOHO*/EIT 171 Å). The probabilities are normalized for period bandwidths covering a factor of 2, i.e., per log $(dT) = 0.3$. Note that the fast-kink MHD mode has the highest probability of coinciding with the 5 minute period, i.e., $\approx 15\%$ within a range $(P + dP)/(P - dP) = 2$, i.e., $T = 3.5$–7.0 minutes or $1/T = 2.3$–4.7 mHz.

consistent with the mean and standard deviations of these parameters. The probability distributions of the four MHD periods are shown in Figure 7, calculated for logarithmic period bins of $d \log P = 0.3$, which corresponds to a period variation by a factor of $(P + dP)/(P - dP) = 10^{0.3} = 2$.

In Figure 7 we indicate the range of measured photospheric "5 minute" oscillation periods, i.e., $P = 220$–400 s. We find that about 15% of all loops in the representative fast kink mode distribution have periods in the photospheric 5 minute range. This number is about 4% for the fast sausage mode, 2% for the fast propagating mode, and almost zero for the slow mode. The fast kink mode would therefore be most likely to couple with photospheric 5 minute oscillations. Note, the *observed* resonant fraction will be less than the 15% predicted, since additional conditions must be fulfilled for the oscillating loops to be detected: (1) a significant amount of energy has to be transferred from the photosphere to the coronal part of the loop for excitation of lateral kink oscillations, (2) the emission measure contrast with respect to the background has to exceed the detection threshold, and (3) the loop temperature has to be close to the peak of the instrumental response function.

4. FLARE-RELATED DISTURBANCES TO THE EUV-EMITTING PLASMA

To give a broader context for the loop oscillations we describe some other dynamical processes that occur during this flare. First, we discuss the nature of the signal or front that appears to trigger the observed position and brightness changes in the active region. Second, we briefly describe the accompanying coronal dimming during and after the flare.

As mentioned earlier, there is a propagating signal or front that expands through the flare volume, which we suggest could be a pressure perturbation, or it could be the response of the flare volume to changes in the magnetic field near the flare site. The observed motion of the loops is consistent with both, but there are also detectable intensity increases in some of the moving loops. Although more careful analysis is necessary to say for certain, we do not think that these increases are due to heating (see § 2.5). This suggests that the brightness increase is likely due to a density increase, which could be manifested in the form of a compression front. There is no such immediate explanation for the intensity increase if all that propagates is a signal.

A signal that the magnetic field has reconfigured would travel through the coronal plasma at the fast magnetoacoustic speed, and a compression front or shock should be traveling faster than this. The fast magnetoacoustic speed is relevant for the propagation of disturbances (such as the observed loop displacements) in the direction perpendicular to the magnetic field. It is given by (e.g., Benz 1993, p. 240)

$$v_{\rm ma}^2 = c_0^2 + v_{\rm A}^2 \,. \tag{9}$$

For plasma emitting in the 171 Å filter, at $T_e \approx 1$ MK (corresponding to the peak of the *TRACE* 171 Å filter response function), the sound speed is $c_0 = 1.5 \times 10^4 T_e^{1/2} = 150$ km s^{-1}. Assuming an Alfvén speed of $v_{\rm A} = 2000$–6000 km s^{-1} at the footpoints and 500–1000 km s^{-1} at the loop tops (using extrapolated field strengths from a similar active region; Aschwanden et al. 1999), we can calculate the magnetoacoustic Mach number $M = v/v_{\rm ma}$ of the disturbance (recall, $v \approx 700$ km s^{-1}): at the footpoints, $M \approx 0.1$–0.3, and $M \approx 0.67$–1.3 at the loop top. Therefore, at the loop tops the disturbance is consistent with Alfvénic or mildly super-Alfvénic propagation, and we cannot, on this basis, distinguish between the propagation of a compressional wave or a reconfiguation of the magnetic field. The disturbance speed in the *TRACE* field of view could mean that the disturbance is a weak shock; the speed is comparable to shock speeds inferred from radio type II burst velocities (e.g., Mann, Classen, & Aurass 1995: $v = 300$–800 km s^{-1}). However, no type II burst was reported for this flare (Solar Geophysical Data No. 649, Part I).

If the brightness increase is solely due to a compressional density increase caused by a perturbation traveling perpendicular to the field (i.e., at the tops of the oscillating loops), we would expect the density to be restored to the predisturbance value on a timescale between the fast magnetoacoustic travel time across the loop and the sound travel time along the loop (if the compression were also to result in material displacements along the loop's axis). Given a loop width of ≈ 1000 km, this former timescale is ≈ 1 s, and the loop intensity patently does not return to preflare values on this timescale. The sound travel time along the loop is indicated in the panels on the right-hand column of Figure 5, using the distance from the flare site to the marked positions as an approximation for the loop half-length, and is ≈ 6–10 minutes. Intensity changes in the loops *are* seen on this timescale; however, at the same time a global dimming of the region takes place, as described in the next paragraph.

We also investigated brightness changes of the EUV flux on larger scales and longer timescale in the flaring active region. Figure 8 shows the average EUV brightness in seven selected subzones of the image, each zone having a side length of 35,000 km. Zones 0–3 are located at the four corners of the field of view, zone 4 in the brightest flare kernel, and zones 5–6 at the edges of the active region. The time profiles of the averaged EUV flux in these 7 zones is shown in Figure 8 as function of time. We note that the

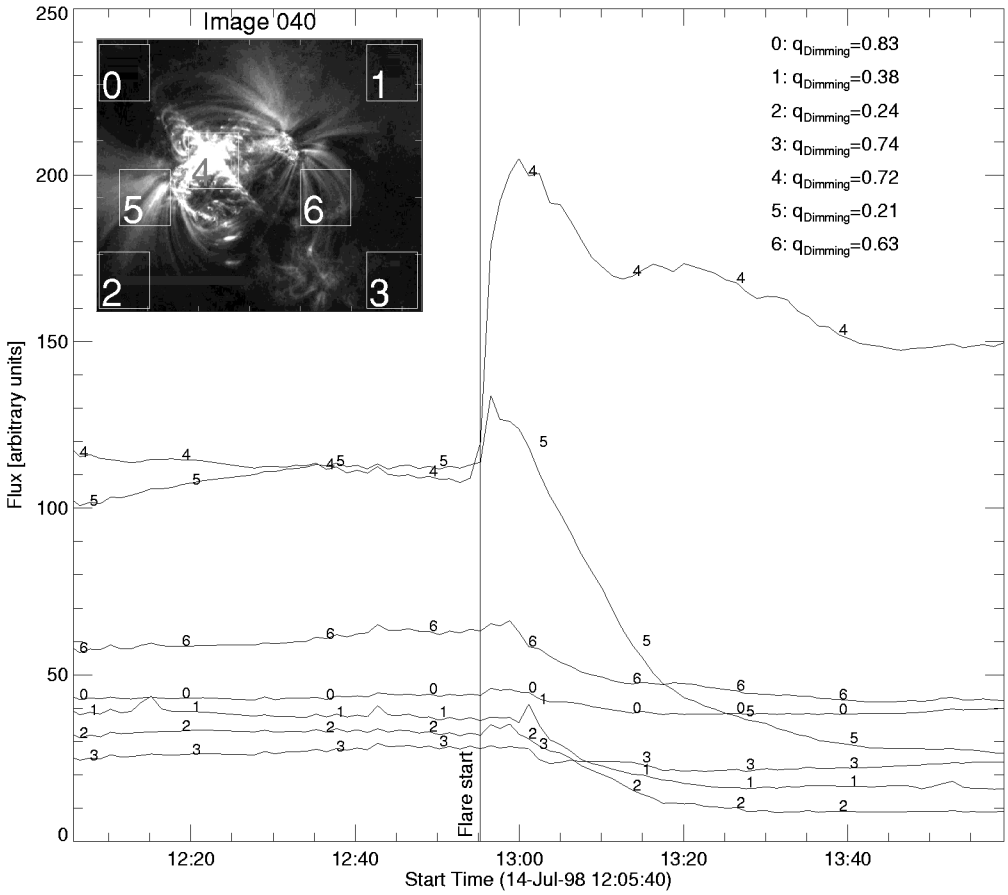

FIG. 8.—Dimming of the EUV brightness is measured in seven locations, averaged over squares of 100 × 100 pixels (with a side length of 35,000 km). The ratio of the dimmed EUV flux during the postflare phase (13:55 UT) to the maximum EUV flux at flare begin (13:00 UT) is indicated in the top right corner. The brightest flare kernel (position 4) dims down to 72% of its peak brightness, while another area (position 6) in the active region dims down to 63%. Note that strongest dimming (down to 21%) outside the active region occurs along a diagonal (positions 2-5-1) that is roughly aligned with the dipole axis of the global field.

EUV brightness is fairly steady (within 10%) in all zones before the flare. At flare start, a maximum brightness increase by a factor of $\approx$2.0 is observed around the main flare kernel C_1 and a small increase by a factor of $\approx$1.2 in zone 5, which connects magnetically with the flare kernel C_3. All other zones show no brightness increase but start to dim about 5 minutes after flare start (12:55 UT). The most dramatic dimming (with respect to the peak flux) occurs in zones 1–2, down to factors of 0.24 and 0.38 of the preflare value. Less dramatic dimming is seen in zones 0, 3, and 6, with factors of 0.83, 0.74, and 0.63, respectively. Interestingly, most of the EUV dimming is seen in the diagonal direction 2-5-1, which is roughly aligned with the global dipole axis of the active region. More specifically, zones 2, 5, and 1 are all located in high-arching or possibly open-field regions of the global dipole field, while all other zones lie above closed-field regions. This finding strongly suggests that the EUV dimming is a direct consequence of coronal mass loss along open field above the flaring region, which opened up after a reconfiguration of the large-scale magnetic field. This phenomenon often accompanies solar flares and has been observed in soft X-rays (Hudson & Webb 1997) and EUV (Thompson et al. 1998). The dimming typically follows the flare and can be associated with a CME (Hudson et al. 1996). In analogy, we associate the observed decrease in EUV brightness here with *coronal dimming* of the rarefied or ejected 1.0–1.5 MK plasma. The timescale of the dimming is about 25 minutes, after which the dim EUV brightness level becomes stabilized. This seems to be the timescale over which a CME clears the field of view, yielding an estimated speed of $v_{CME} \approx$ 200,000 km/1500 s = 130 km s^{-1}. The replenishment or heating of the 1 MK corona and the related restoration of the EUV brightness in the evacuated flare volume seems to take significantly longer than our observing sequence (lasting until $\approx$1.3 hr after the flare).

Previous observations in EUV have shown clear manifestations of CMEs with spherical shock fronts and density voids following behind (e.g., with *SOHO*/EIT observations; Dere et al. 1997; Moses et al. 1997). Some of the CMEs were, as ours is, accompanied by radially propagating disturbances that have tentatively been identified as coronal manifestations of "Moreton waves," with typical speeds of 250–400 km s^{-1} (Thompson et al. 1998). These wave fronts have also been associated with models of weak fast-mode MHD waves (Uchida 1968, 1974). The expanding disturbance we observe here seems to be faster and to lack the well-structured wave front seen in "Moreton wave" events.

5. CONCLUSIONS

We have analyzed spatial oscillations of coronal loops, which could be measured for the first time with *TRACE*.

The oscillating loops were most conspicuous during the first 20 minutes after the flare (1998 July 14, 12:55 UT). The oscillating loops have a mean period of $T = 4.6 \pm 0.4$ minutes and are synchronized within a phase of $\lesssim 20\%$. The amplitude of the transverse loop oscillations is $\approx 3\%$ of the loop length, occurring in large-scale loops ($L \approx 130{,}000$ km) that are significantly larger than the compact SXR-bright flare loops ($L \approx 20{,}000$ km). The flare originates a disturbance that propagates quasi-radially from the central flare site with a projected speed of $v \approx 700$ km s^{-1}. Most of the loops appear to respond to the passage of this disturbance in one way or the other, either by a slight displacement from and return to the original position or by an oscillation around the equilibrium position. The timing of the spatial loop displacements coincides with the arrival time of the disturbance at the loop tops. We observe also a strong EUV dimming in the postflare phase, which seems to be caused by CME along the open field lines anchored in the leading and trailing region of the dipolar active region. The amount of EUV dimming drops in some locations down to 20% of the preflare EUV brightness, suggesting a density reduction by a factor of ≈ 2 after flare start, probably caused by a large-scale CME above the flare site.

Investigating various MHD modes of coronal loops, we find that the observed periods of the asymmetric, sinusoidal displacements are most consistent with the fast kink mode. We find little phase shift along the loops, implying a standing wave mode with fixed nodes.

Because of the coincidence with the photospheric 5 minute period, a coupling between a photospheric driver and a coronal loop mode is considered. Based on statistical parameters of electron densities, magnetic fields, and loop heights that are typical for 1.0–1.5 MK loops observed at a wavelength of 171 Å by *SOHO*/EIT, we find that a fraction up to $\approx 15\%$ of loops in the group may be in resonance with a 5 minute driver.

The discovery of *spatial* loop oscillations has important consequences. (1) The fast MHD kink mode provides a new diagnostic of the coronal magnetic field. Because loop lengths and coronal densities can be determined with current techniques, the MHD kink mode period provides a unique constraint for the magnetic field strength of a resonant loop segment. (2) The measurement of spatial displacements of coronal loops can be used to probe physical parameters (timing, velocity, density compression) of flare-induced disturbances (e.g., Alfvénic MHD waves, shock waves, Moreton waves). Further *TRACE* observations with higher cadences would be most useful to pursue such dynamical studies. (3) The photospheric 5 minute oscillation may amplify coronal loop oscillations, leading us to suggest that other coronal oscillations could be clustered around the 5 minute period.

We thank the referee, Joe Gurman, for insightful comments on the manuscript. We acknowledge helpful discussions with Alan Title, Dick Shine, Ted Tarbell, Leon Golub, and David McKenzie and thank the *TRACE* team for assistance in data processing. The *TRACE* team includes scientists from Lockheed Martin Advanced Technology Center, Stanford University, NASA Goddard Space Flight Center, the University of Chicago, Montana State University, and the Harvard-Smithsonian Center for Astrophysics. The *Yohkoh*/SXT data used in this paper were taken by the *Yohkoh* mission of ISAS, Japan, which was prepared and is operated by the international collaboration of Japanese, US, and UK scientists under the support of ISAS, NASA, and PPARC, respectively.

REFERENCES

Abrami, A. 1970, Sol. Phys., 11, 104
———. 1972, Nature Phys. Sci., 238(80), 25
Abrami, A., & Koren, U. 1978, A&AS, 34, 165
Achong, A. 1974, Sol. Phys., 37, 477
Antonucci, E., Gabriel, A. H., & Patchett, B. E. 1984, Sol. Phys., 93, 85
Aschwanden, M. J. 1986, Sol. Phys., 104, 57
———. 1987a, Sol. Phys., 111, 113
———. 1987b, Ph.D. thesis, ETH Zurich, Switzerland
Aschwanden, M. J., Bastian, T. S., & Gary, D. E. 1992, BAAS, 24/2, 802
Aschwanden, M. J., Benz, A. O., Dennis, B. R., & Gaizauskas, V. 1993, ApJ, 416, 857
Aschwanden, M. J., Benz, A. O., Dennis, B. R., & Kundu, M. K. 1994b, ApJS, 90, 631
Aschwanden, M. J., Benz, A. O., & Montello, M. L. 1994a, ApJ, 431, 432
Aschwanden, M. J., Dennis, B. R., & Benz, A. O. 1998, ApJ, 497, 972
Aschwanden, M. J., Newmark, J. S., Delaboudiniere, J. P., Neupert, W. M., Klimchuk, J. A., Gary, G. A., Portier-Fornazzi, F., & Zucker, A. 1999, ApJ, 515, 842
Aurass, H., Chernov, G. P., Karlicky, M., Kurths, J., & Mann, G. 1987, Sol. Phys., 112, 347
Aurass, H., & Mann, G. 1987, Sol. Phys., 112, 359
Baranov, N. V., & Tsvetkov, L. I. 1994, Astron. Lett., 20/3, 327
Benz, A. O. 1993, Plasma Astrophysics (Dordrecht: Kluwer)
Berghmans, D., & DeBruyne, P. 1995, ApJ, 453, 495
Bernold, T. E. X. 1980, A&AS, 42, 43
Bocchia, R., & Puomeyrol, F. 1974, Sol. Phys., 38, 193
Cargill, P. J., Chen, J., & Garren, D. A. 1994, ApJ, 423, 854
Cheng, C. C. 1977, ApJ, 213, 558
Chernov, G. P., Markeev, A. K., Poquerusse, M., Bougeret, J. L., Klein, K. L., Mann, G., Aurass, H., & Aschwanden, M. J. 1998, A&A, 334, 314
Correia, E., & Kaufmann, P. 1987, Sol. Phys., 111, 143
Costa, J. E. R., & Kaufmann, P. 1986, Sol. Phys., 104, 253
DeForest, D. E., & Gurman, J. B. 1998, ApJ, 501, L217
DeGroot, T. 1970, Sol. Phys., 14, 176
Dere, K. P., et al. 1997, Sol. Phys., 175, 601
Desai, U. D., Kouveliotou, C., Barat, C., Hurley, N., Niel, M., Talon, R., & Vedrenne, G. 1987, in Rapid Fluctuations in Solar Flares, ed. B. R. Dennis, L. E. Orwig, & A. L. Kiplinger (NASA CP 2449), 63
Deubner, F., & Gough, D. 1984, ARA&A, 22, 593
Dröge, F. 1967, Z. Astrophys., 66, 200
Edwin, P., & Roberts, B. 1983, Sol. Phys., 88, 179
Elgarøy, Ø. 1980, A&A, 82, 308
Elgarøy, Ø., & Sveen, O. P. 1973, Sol. Phys., 32, 231
Foukal, P. 1990, Solar Astrophysics (New York: Wiley)
Fu, Q. J., Gong, Y. F., Jin, S. Z., & Zhao, R. Y. 1990, Sol. Phys., 130, 161
Gotwols, B. L. 1972, Sol. Phys., 25, 232
Handy, B., et al. 1999, Sol. Phys., submitted
Harrison, R. A. 1987, A&A, 182, 337
Hudson, H. S., Acton, L. W., Alexander, D., Freeland, S. L., Lemen, J. R., & Harvey, K. L. 1996, in AIP Conf. Proc. 382, Proc. 8th International Solar Wind Conf., ed. D. Winterhalter, J. T. Gosling, S. R. Habbal, W. S. Kurth, & M. Neugebauer (New York: AIP), 88
Hudson, H. S., & Webb, D. 1997, in Coronal Mass Ejections, ed. N. U. Crooker, J. Joselyn, & J. Feynman (Washington, DC: AGU), 27
Jain, R., & Tripathy, S. C. 1998, Sol. Phys., 181, 113
Janssens, T. J., & White, K. P., III. 1969, ApJ, 158, L127
Joarder, P. S., Nakariakov, V. M., & Roberts, B. 1997, Sol. Phys., 173, 81
Kattenberg, A., & Kuperus, M. 1983, Sol. Phys., 85, 185
Kaufmann, P. 1972, Sol. Phys., 23, 178
Kiplinger, A. L., Dennis, B. R., Frost, K. J., & Orwig, L. E. 1983, ApJ, 273, 783
Koutchmy, S., Zhugzhda, Y. D., & Locans, V. 1983, A&A, 120, 185
Kurths, J., Benz, A. O., & Aschwanden, M. J. 1991, A&A, 248, 270
Kurths, J., & Herzel, H. P. 1986, Sol. Phys., 107, 39
Kurths, J., & Karlicky, M. 1989, Sol. Phys., 119, 399
Leighton, R. B., Noyes, R. W., & Simon, G. W. 1962, ApJ, 135, 474
Lipa, B. 1978, Sol. Phys., 57, 191
Lites, B. W. 1992, in NATO ASI Ser. C, Mathematical and Physical Sciences 375, ed. J. H. Thomas & N. O. Weiss (Dordrecht: Kluwer), 261
Mann, G., Classen, T., & Aurass, H. 1995, A&A, 295, 775
McLean, D. J., & Sheridan, K. V. 1973, Sol. Phys., 32, 485
McLean, D. J., Sheridan, K. V., Stewart, R. T., & Wild, J. P. 1971, Nature, 234, 140
McKenzie, D. E. 1997, PASP, 109, 739
McKenzie, D. E., & Mullan, D. S. 1997, Sol. Phys., 176, 127
Moses, D., et al. 1997, Sol. Phys., 175, 571

Murawski, K., Aschwanden, M. J., & Smith, J. M. 1998, Sol. Phys., 179, 313
Parks, G. K., & Winckler, J. R. 1969, ApJ, 155, L117
Pasachoff, J. M., & Ladd, E. F. 1987, Sol. Phys., 109, 365
Pasachoff, J. M., & Landman, D. A. 1984, Sol. Phys., 90, 325
Pick, M., & Trottet, G. 1978, Sol. Phys., 60, 353
Qin, Z., & Guang-Li, H. 1994, Ap&SS, 218, 213
Qin, Z., Li, C., & Fu, Q. 1996, Sol. Phys., 163, 383
Roberts, B., Edwin, P., & Benz, A. O. 1984, ApJ, 279, 857
Rosenberg, H. 1970, A&A, 9, 159
———. 1972, Sol. Phys., 25, 188
Sastry, Ch. V., Krishan, V., & Subramanian, K. R. 1981, J. Astrophys. Astron., 2, 59
Schrijver, C., et al. 1999, Sol. Phys., in press
Simon, M., & Shimabukuro, F. I. 1971, ApJ, 168, 525
Slottje, C. 1981, Atlas of Fine Structures of Dynamic Spectra of Solar Type IV-dm and Some Type II Radio Bursts (Dwingeloo)
Steinolfson, R. S., & Davila, J. M. 1993, ApJ, 415, 354
Strauss, F. M., Kaufmann, P., & Opher, R. 1980, Sol. Phys., 67, 83
Svestka, Z. 1994, Sol. Phys., 152, 505
Takakura, T., Kaufmann, P., Costa, J. E. R., Degaonkar, S. S., Ohki, K., & Nitta, N. 1983, Nature, 302, 5906
Tapping, K. F. 1978, Sol. Phys., 59, 145
Tarbell, T. D., et al. 1994, in Proc. 3d *SOHO* Workshop, Solar Dynamic Phenomena and Solar Wind Consequences (ESA SP-373; Paris: ESA), 375
Thomas, J. H. 1981, in The Physics of Sunspots, ed. L. E. Cram & J. H. Thomas (Sunspot: Sacramento Peak Observatory), 345
Thomas, R. J., Neupert, W. M., & Thompson, W. T. 1987, in NASA Conf. Proc. 2449, Rapid Fluctuations in Solar Flares, ed. B. R. Dennis, L. E. Orwig, & A. L. Kiplinger (Washington, DC: NASA), 299
Thompson, B. J., Plunkett, S. P., Gurman, J. B., Newmark, J. S., St. Cyr, O. C., Michels, D. J., & Delaboudinière, J.-P. 1998, Geophys. Res. Lett., 25/14, 2461
Trottet, G., Kerdraon, A., Benz, A. O., & Treumann, R. 1981, A&A, 93, 129
Trottet, G., Pick, M., & Heyvaerts, J. 1979, A&A, 79, 164
Uchida, Y. 1968, Sol. Phys., 4, 30
———. 1974, Sol. Phys., 39, 431
Wang, M., & Xie, R. X. 1997, Sol. Phys., 176, 171
Wentzel, D. G. 1979, ApJ, 227, 319
Wiehl, H. J., Benz, A. O., & Aschwanden, M. J. 1985, Sol. Phys., 95, 167
Zaitsev, V. V., Stepanov, A. V., & Chernov, G. P. 1984, Sol. Phys., 93, 363
Zlobec, P., Messerotti, P., Dulk, G. A., & Kucera, T. 1992, Sol. Phys., 141, 165
Zodi, A. M., Kaufmann, P., & Zirin, H. 1984, Sol. Phys., 92, 283